



1    Analysis of 24 years of mesopause region OH rotational temperature  
2    observations at Davis, Antarctica. Part 1: Long-term trends.

3

4    W. John R. French<sup>1</sup>, Frank J. Mulligan<sup>2</sup>, and Andrew R. Klekociuk<sup>1,3</sup>

5

6    <sup>1</sup>Australian Antarctic Division, 203 Channel Hwy, Kingston, Tasmania, 7050, Australia

7    <sup>2</sup>Maynooth University, Maynooth, Co. Kildare, Ireland

8    <sup>3</sup>Department of Physics, University of Adelaide, Adelaide, 5005, Australia

9

10    *Correspondence to:* W. John R. French (john.french@aad.gov.au)

11



## 12 Abstract

13           The long term trend, solar cycle response and residual variability in 24 years of  
14 hydroxyl nightglow rotational temperatures above Davis Research Station, Antarctica (68°  
15 S, 78° E) is reported. Hydroxyl rotational temperatures are a layer-weighted proxy for  
16 kinetic temperatures near 87 km altitude and have been used for many decades to monitor  
17 trends in the mesopause region in response to increasing greenhouse gas emissions.  
18 Routine observations of the OH(6-2) band P-branch emission lines using a scanning  
19 spectrometer at Davis station have been made continuously over each winter season since  
20 1995. Significant outcomes of this most recent analysis update are (a) a record low winter-  
21 average temperature of 198.3 K is obtained for 2018 (1.7 K below previous low in 2009)  
22 (b) a long term cooling trend of 1.2 K/decade persists, coupled with a solar cycle response  
23 of 4.3 K/100 solar flux units and (c) we find evidence in the residual winter mean  
24 temperatures of an oscillation on a quasi-quadrennial (QQO) timescale which is  
25 investigated in detail in part 2 of this work.

26           Our observations and trend analyses are compared with satellite measurements  
27 from Aura/MLS version v4.2 level 2 data over the last 14 years and we find close agreement  
28 (a best fit) with the 0.00464 hPa pressure level values. The solar cycle response, long-term  
29 trend and underlying QQO residuals are consistent with the Davis observations.  
30 Consequently, we extend the Aura/MLS trend analysis to provide a global view of solar  
31 response and long term trend for southern and northern hemisphere winter season to  
32 compare with other observers and models.

33

34

35



## 1. Introduction

Long-term monitoring of basic atmospheric parameters is fundamentally important to understand natural, periodic and episodic variability in atmospheric processes, to provide data to verify increasingly sophisticated atmospheric models and to resolve and quantify perturbations due to global change on decadal to century timescales. Dynamical processes, including gravity waves, tides, planetary waves, large scale circulation patterns and quasi-periodic teleconnections (such as the quasi-biennial oscillation (QBO), El Niño Southern Oscillation (ENSO), and the Pacific Decadal Oscillation (PDO)), changes to the chemical composition and radiative balance (particularly due to anthropogenic emissions of greenhouse and chlorofluorocarbon gasses) and external forcing such as the 27-day solar rotation and 11-year solar activity cycle, all play significant roles (directly and through interactions) in defining and perturbing the mean state of the atmosphere. Decades of well calibrated measurements are required to accurately quantify variations and trends on these timescales.

Meteorological reanalyses derived from assimilation of a vast number of surface observations provide time-series for useful trend analyses for the lower atmosphere e.g. (Bengtsson et al., 2004). A few satellite based data sets are now also reaching multi-decadal timescales (e.g. the Thermosphere Ionosphere Mesosphere Energetics Dynamics satellite's Sounding of the Atmosphere using Broadband Emission Radiometry instrument (TIMED)/SABER) (Mertens et al., 2003), and the Earth Observing System satellite Aura Microwave Limb Sounder (Aura/MLS) (Schwartz et al., 2008), that extend observations to the upper atmosphere. Of current and particular interest to climate science in the modern era are the atmospheric temperature trends in response to increasing global greenhouse gas emissions, principally from carbon dioxide (CO<sub>2</sub>). Modelling studies over many years suggest that the sensitivity to CO<sub>2</sub> changes in the upper atmosphere, particularly at high latitudes, is



61 much larger than in the lower atmosphere (e.g. Roble (2000), the Canadian Middle  
62 Atmosphere Model (CMAM) (Fomichev et al., 2007)) and the Hamburg Model of the  
63 Neutral and Ionized Atmosphere (HAMMONIA) (Schmidt et al., 2006)).

64 Above the stratosphere, the low collision frequency means that CO<sub>2</sub> preferentially  
65 radiates absorbed energy to space, resulting in a net cooling. Thus, the expected long-term  
66 temperature trends in the mesosphere and lower thermosphere due to CO<sub>2</sub> are negative.  
67 Ground based optical measurements of the Meinel emission bands of the hydroxyl (OH)  
68 molecule produced by the exothermic hydrogen (H) – ozone (O<sub>3</sub>) reaction ( $\text{H} + \text{O}_3 \rightarrow \text{OH}^* + 3.34 \text{ eV}$ )  
69 have been used extensively over almost six decades as a method of measuring  
70 atmospheric temperature in the vicinity of the mesopause (Kvifte, 1961; Sivjee, 1992; Beig  
71 et al. 2003; Beig 2006; Beig et al. 2008; Beig 2011). The emission is centred about 87 km  
72 altitude and the rotational temperatures derived are representative of the kinetic  
73 temperatures, weighted by the shape and width of the layer (~8 km full-width at half-  
74 maximum (FWHM)). Temperatures thus obtained have always been considered ambiguous  
75 to the extent that they are dependent on the altitude of the emitting layer, and they are  
76 weighted by the altitude profile of that layer. In the case of the OH\* layer, different  
77 vibrational bands are known to be weighted towards different altitude layers (von Savigny  
78 et al. 2012), and on short time scales, individual bands vary in altitude with diurnal, semi-  
79 diurnal, annual, semi-annual and solar cycle variations (García-Comas et al., 2017; Liu and  
80 Shepherd, 2006; Mulligan et al., 2009). Over long timescales (more than one solar cycle)  
81 however, recent studies using satellite data (Gao et al., 2016; von Savigny, 2015) and OH  
82 Chemistry-Dynamics (OHCD) models have shown that, the OH\* layer altitude is  
83 remarkably insensitive to changes in CO<sub>2</sub> concentration or solar cycle variation. This  
84 makes these measurements very valuable for monitoring long term changes in the  
85 atmosphere.



86           This work provides an update on the solar cycle and long term trend analysis of the  
87   OH rotational temperature measurements taken through each winter season at Davis  
88   Research Station, Antarctica. The dataset used here extends for 24 consecutive years and  
89   this analysis includes a further 8 years of measurements since the previously published  
90   trend assessment using these data ( French and Klekociuk, 2011). Here we expand on the  
91   earlier analysis to provide a more detailed assessment of the solar response, trends and  
92   variability in the Davis record in comparison with v4.2 measurements from the Microwave  
93   Limb Sounder (MLS) on the Aura satellite (Aura/MLS) and a network of similar ground  
94   based observations (coordinated by the Network for Detection of Mesospheric Change,  
95   (NDMC) Reisin et al. 2014).

96           The outline of this paper is as follows. The instrumentation used and the acquired  
97   rotational temperature data collection are presented in Sections 2 and 3. Analysis of solar  
98   cycle response and the long-term linear trend is undertaken in Section 4 including  
99   comparisons with other ground-based observers and satellite measurements. Discussion of  
100   the results, summary and conclusions drawn are given in Sections 5 and 6, respectively.  
101   We use the following terminology for the analysed temperature series in this manuscript.  
102   From the measured temperatures and their nightly, monthly, seasonal or winter means,  
103   *temperature anomalies* are produced by subtracting the climatological mean or monthly  
104   mean (we fit solar cycle and linear trend to the anomalies), *residual temperatures*  
105   additionally have the solar cycle component subtracted (used in discussion of long-term  
106   trends) and *detrended temperatures* additionally have the long term linear trend subtracted  
107   (used in discussion about remaining variability).

108



## 109 2. Instrumentation

110 A SPEX Industries Czerny-Turner grating spectrometer of 1.26 m focal length has  
111 been used to autonomously scan the OH(6-2) P-branch emission spectra ( $\lambda$ 839-851 nm) at  
112 Davis (68.6° S, 78.0° E) each winter season over the last 24 years (1995-2018). Night-time  
113 observations (sun > 8° below the horizon) are only possible between mid-February (~day  
114 048) and end of October (~day 300) at Davis.

115 The spectrometer views the sky in the zenith with a 5.3° field-of-view and an  
116 instrument resolution of ~0.16 nm, sufficient to separate P<sub>1</sub> and P<sub>2</sub> branch lines but not to  
117 resolve their Lambda-doubling components. Observations are made regardless of cloud or  
118 moon conditions and take of the order of 7 minutes to acquire a complete spectrum.

119 Spectral response calibration has been maintained by reference to several tungsten filament  
120 Low Brightness Source units (a total of 4164 scans over the 24 years at Davis) which are  
121 in turn cross referenced to national standard lamps at the Australian National Measurement  
122 Institute (a total of 781 cross reference calibrations over 24 years). The response correction  
123 accounts mainly for the fall-off in response of the cooled gallium arsenide (GaAs)  
124 photomultiplier detector and amounts to 8.5% between the P<sub>1</sub>(2) and P<sub>1</sub>(5) of the OH(6-2)  
125 band. The total change in spectral response correction over 24 years is less than 0.3%  
126 (equates to less than 0.3 K for the P<sub>1</sub>(2) / P<sub>1</sub>(5) ratio) despite changing the diffraction grating  
127 in 2006 and four changes of the GaAs photomultiplier detector which are carefully  
128 characterised over the years. The assigned annual calibration uncertainty is generally <0.3  
129 K except for 1995 (1.8 K) due to calibration via a secondary calibration lamp and in 2002  
130 (1.2 K) due to detector cooling problems. Further details of the instrument are contained in  
131 Greet et al. (1997) and French et al. (2000).

132



### 133 3. Davis 24 year rotational temperature dataset

134 We use the three possible ratios from the  $P_1(2)$ ,  $P_1(4)$  and  $P_1(5)$  emission line  
135 intensities to derive a weighted mean temperature. Intensity values are interpolated to a  
136 common time between consecutive spectra to reduce errors associated with the 7 minute  
137 acquisition cycle time. The weighting factor is the statistical counting error (based on the  
138 error in estimating each line intensity).  $P_1(2)$  is corrected for the ~2% contribution by  $Q_1(5)$ .  
139 Line backgrounds are selected to balance the small auroral contribution of the N21PG and  
140  $N_2^+$  Meinel bands and solar Fraunhofer absorption for spectra acquired under moonlit  
141 conditions. Correction factors account for the difference in Lambda-doubling between the  
142 P-branch lines determined with knowledge of the instrument line shape from high-  
143 resolution scans of a frequency-stabilized laser.

144 Langhoff et al. (1986) transition probabilities are used to derive rotational  
145 temperatures (see French et al., 2000). Other published sets (e.g., Mies, 1974; Turnbull  
146 and Lowe, 1989; van der Loo and Groenenboom, 2007; Brooke et al., 2016) can change  
147 the absolute temperatures derived by up to 12 K, but does not significantly affect the trend  
148 analysis reported here. It should be noted however that comparison of absolute  
149 temperatures with other observations are significantly affected by different choices of  
150 transition probabilities.

151 Selection criteria limit extreme values of weighted standard deviation and counting  
152 error, slope and magnitude of the background and the rate of change of branch line  
153 intensities between consecutive scans. Further details of the rotational temperature analysis  
154 procedure are available in Burns et al. (2003) and French and Burns (2004).

155 Of over 624,000 measurements (typically ~26,000 profiles/year), 403,437 derived  
156 temperatures pass reasonably tight selection criteria (many low signal-to-noise ratio  
157 profiles taken through thick cloud or high background profiles around full moon are



158 rejected). These yield 5,309 nightly mean temperatures, where there are at least 10 valid  
159 samples that contribute within  $\pm 12$  hours of local midnight ( $\sim 1850$  Universal Time (UT)).  
160 The time series spans two solar cycles (cycles 23 and 24) with peaks in 2001 and 2014.  
161 Annual mean temperatures show a dependence on solar activity (see French and Klekociuk  
162 (2011) for a comparison of different measures of solar activity with the Davis OH  
163 temperature data). We use the 10.7 cm solar radio flux index (F10.7; 1 solar flux unit (sfu)  
164  $= 10^{-22} \text{ W m}^{-2} \text{ Hz}^{-1}$ ) as our preferred measure of solar activity (F10.7 is fitted and subtracted  
165 to examine residual variability). A plot of the nightly and winter mean temperatures with  
166 the F10.7 time series used in this work is provided in Fig. 1.

167

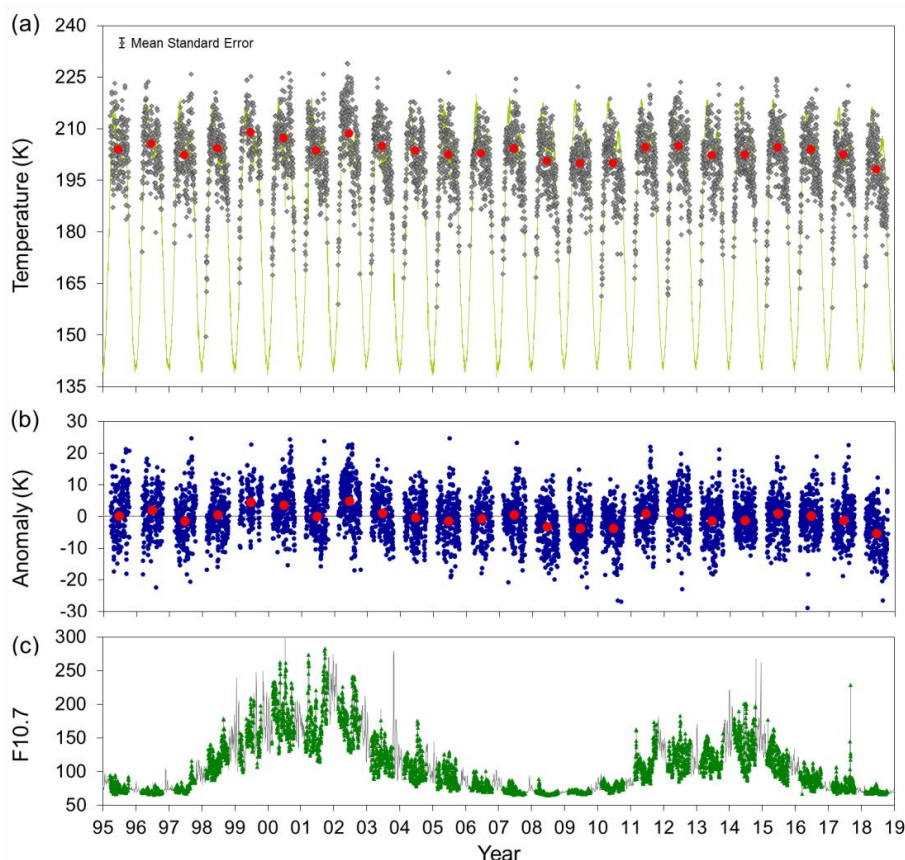


Figure 1 (a). Davis nightly mean temperatures (grey dots; 5309 samples) and winter mean temperatures (D106-259; red points) plotted over the MSISE90 model temperature for 68°S for seasonal reference (Hedin, 1991). (b). nightly mean and winter mean temperature anomalies derived by subtracting the climatological mean (see text) and (c). Daily mean F10.7 cm solar flux index (green points correspond to Davis OH temperature samples)

A climatological mean is derived from a fit to the superposition of nightly mean temperatures for all annual series. The climatological mean is characterised by a rapid autumn transition (February-March) increasing at 1.2 K/day until a turn-over about 29 March (day of year D088), a slow winter decline (April-September) of -0.4 K/day that is punctuated by mid-April (~D113) and mid-August (~D227) dips corresponding to reversals in the mean meridional flow (Murphy et al., 2007), followed by a rapid spring transition (October-November) of -1.0 K/day. Figure 2 shows the superposed nightly



means for each year and the climatological mean fit. Subtracting the climatological mean produces 5309 nightly mean temperature anomalies. Winter mean temperatures are calculated over the interval from 15 April (D106) to 15 September (D259) which avoids the winter to summer transition intervals and lower numbers of nightly observations due to the shorter night length.

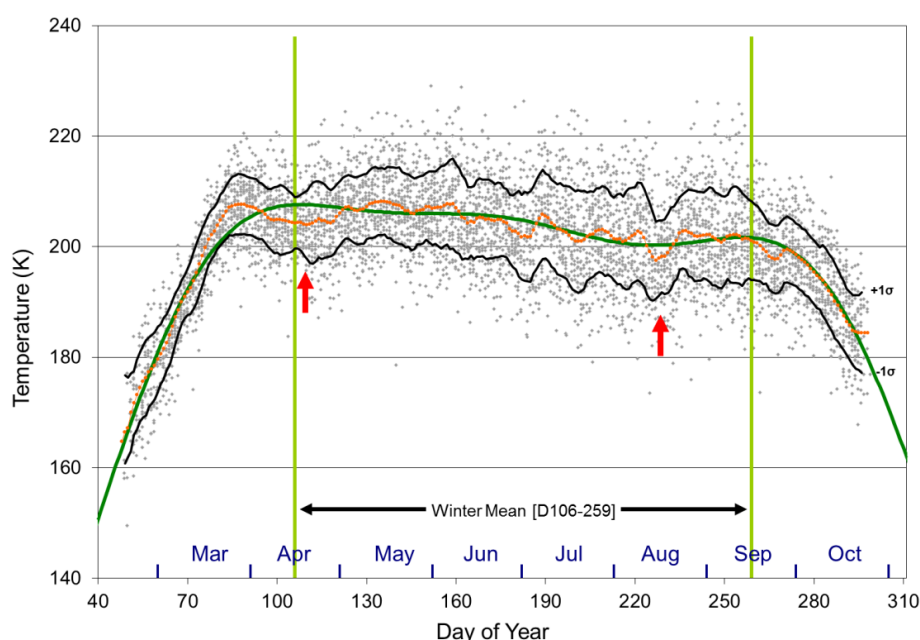


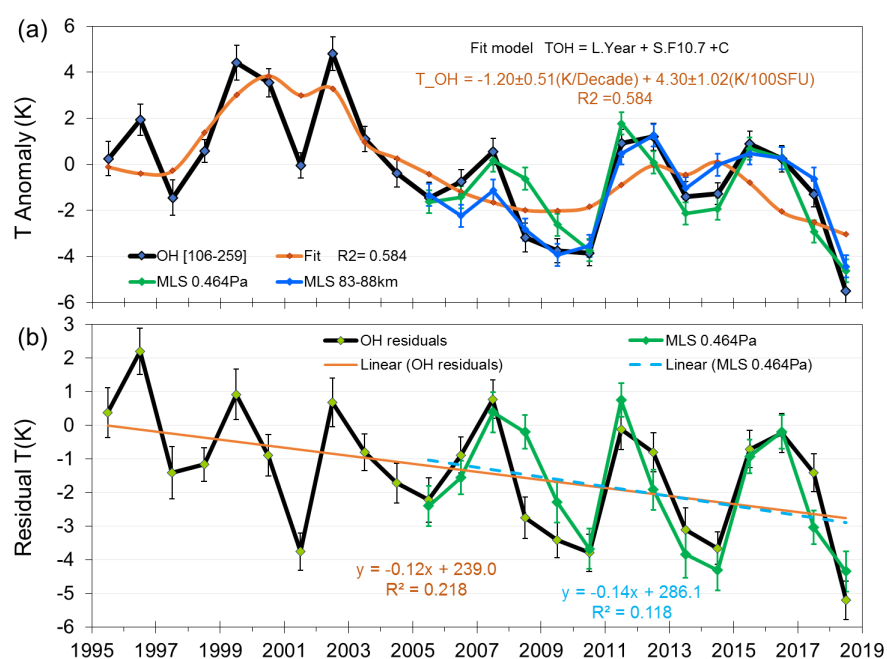
Figure 2. Superposed nightly mean temperatures from 1995 to 2018 [gray points] and a 5-day running mean which represents the climatological mean [orange line] with 1σ intervals [black lines]. The seasonal variation [green annual, semi-annual, ter-annual fit] is characterised by a rapid autumn transition (Feb-Mar) increasing at 1.2 K/day until a turn-over about 29<sup>th</sup>-March (day 088), a slow winter decline (Apr-Sep) of -0.4 K/day, punctuated by mid-April and mid-August dips [indicated by red arrows], followed by a rapid spring transition (Oct-Nov) of -1.0 K/day. Green vertical lines mark the calculation region for winter mean temperatures (outside the winter to summer transition intervals).



## 201 4. Trend Assessment

### 202 4.1 Davis winter mean trends

203 Winter mean temperature anomalies over the 24 years of observations are plotted  
 204 in Fig. 3a. The time series is fitted with a linear model containing a solar cycle term (F10.7)  
 205 and long term linear trend. This model yields a solar cycle response coefficient of  $4.30 \pm$   
 206  $1.02 \text{ K/100sfu}$  (95% confidence limits  $2.2 \text{ K/100sfu} < S < 6.4 \text{ K/100sfu}$ ) and a long term  
 207 linear trend of  $-1.20 \pm 0.51 \text{ K/decade}$  (95% confidence limits  $-0.14 \text{ K/decade} < L < -2.26$   
 208  $\text{K/decade}$ ) and accounts for 58% of the temperature variability.



209 Figure 3 (a). Winter mean (D106-259) temperature anomalies (black line) for Davis  
 210 station ( $68^\circ\text{S}$ ,  $78^\circ\text{E}$ ) fitted with a linear model containing a solar cycle term (F10.7cm flux)  
 211 and long term linear trend (orange line). Fit coefficients are  $4.30 \pm 1.02 \text{ K/100sfu}$  (95%  
 212 confidence limits 2.18 to 6.42 K/100sfu) and  $-1.20 \pm 0.51 \text{ K/decade}$  (95% confidence limits  
 213  $-0.14$  to  $-2.26 \text{ K/decade}$ ) respectively and account for 58% of the temperature variability.  
 214 Also plotted (from 2005) are Aura/MLS temperature anomalies derived from the AMJJAS  
 215 means of all satellite observations within 500 km of Davis station. (b) As for (a), but with  
 216 the solar cycle component removed to better reveal the long term trend and quasi-  
 217 quadrennial oscillation (QOO). OH residuals (black line) are compared with Aura/MLS  
 218 temperature residuals at the 0.0046 hPa level, corrected with the same solar cycle  
 219 component as used for the Davis OH measurements.  
 220



221 We note that a new record low winter-mean temperature was set for the Davis  
222 measurements in 2018, with a value of 198.3 K, which is 1.7 K below the previous  
223 minimum recorded in 2009 (200.0 K). This is not entirely due to the low solar activity in  
224 2018 (winter mean flux of 70.4 sfu) as both 2008 (66.9 sfu) and 2009 (69.1 sfu) had lower  
225 mean flux and comparable years 1996 (70.6 sfu) was 7.4 K warmer (205.7 K) and 2007  
226 (71.9 sfu) was 6.1 K warmer (204.4 K).

227 Extracting the solar cycle contribution from the time series yields the long term  
228 linear trend and residual variability plotted in Fig. 3b. It is apparent from this plot that a  
229 significant oscillation on an approximately 4-year (quasi-quadrennial) timescale remains.  
230 A least-squares fit of a sinusoidal function to the data yields a period of 4.2 years and peak-  
231 peak amplitude of  $\sim 3$  K. This feature will be examined in detail in Part 2 of this work  
232 (French et al., 2019).

233 Distributions of the nightly mean residual temperatures for each year are shown for  
234 comparison in Fig. 4. Histogram colour scale indicates the winter mean temperature from  
235 warmest year (1999; red) to coldest year (2018; blue). Distributions vary between years  
236 from sharp normal distributions (e.g., 1998, 2007, 2016), to broad flat distributions (e.g.,  
237 1996, 1997), to skewed or double peaked distributions (e.g., 2004, 2012, 2014, 2018).  
238 These differences can be attributed to the variability in large scale planetary wave activity  
239 from year to year (French and Klekociuk, 2011)

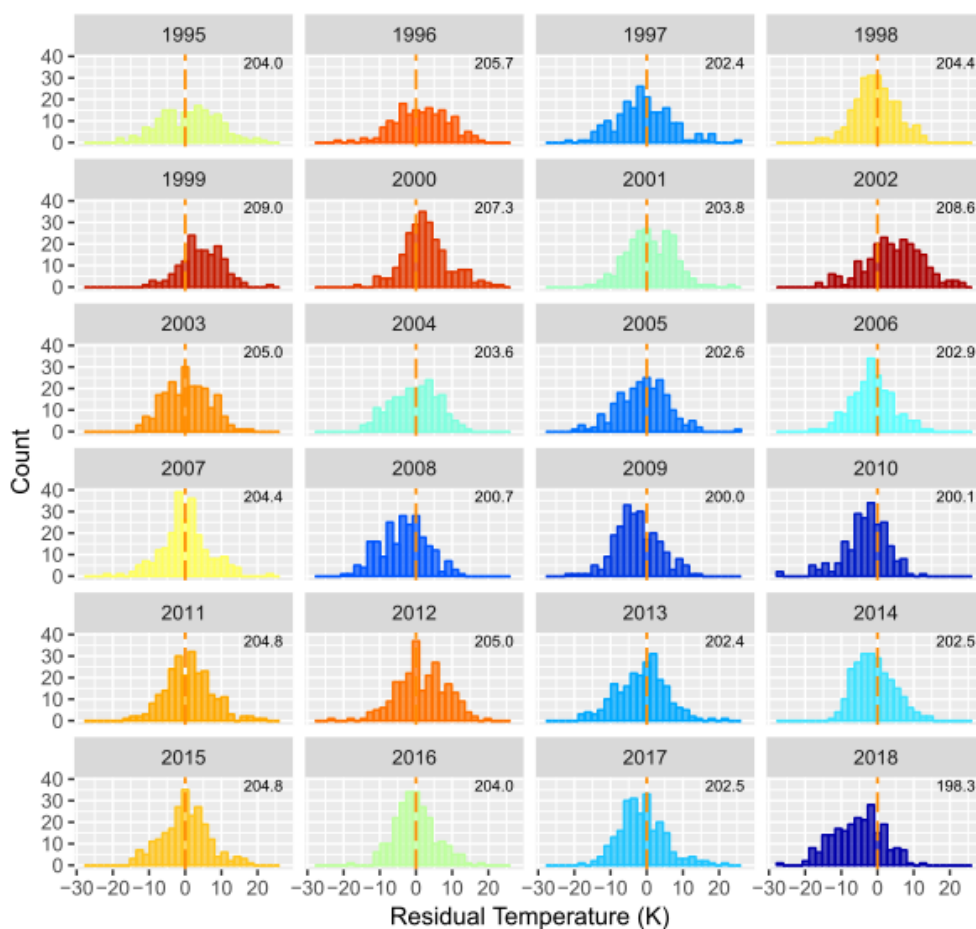


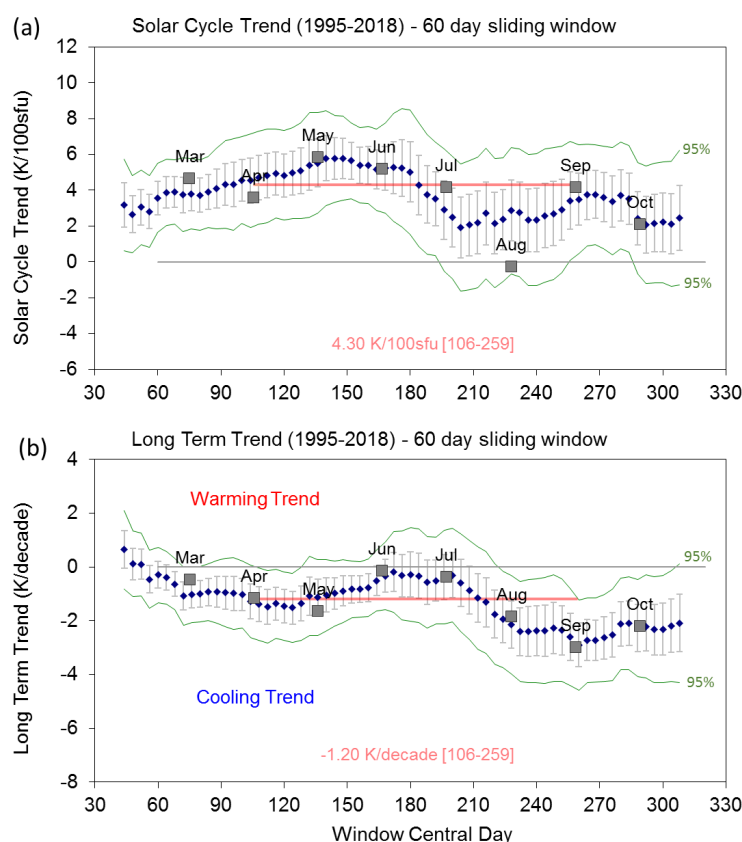
Figure 4. Histograms of nightly mean residual temperatures showing the distribution about the mean winter temperature (annotated in top right corner) coloured from red (warmest year: 1999) to blue (coldest year: 2018).

#### 4.2 Seasonal variability in trends.

Seasonal trend coefficients are also somewhat variable. Figure 5 shows the seasonal variability in solar cycle and long-term trend coefficients derived using a 60 day sliding window, and as monthly trends, compared to the winter mean trends (red lines) derived for Fig. 3. Seasonal solar response shows a maximum in May-June ( $\sim 5$  K/100sfu) and minimum around August ( $\sim 2$  K/100sfu). Note that April and August temperatures are affected by the characteristic dips seen in the climatological mean during these months (see



252 Fig. 2). Linear trend coefficients show maximum cooling responses in April-May ( $\sim -1.3$   
 253 K/decade) and in August-October ( $\sim -2.5$  K/decade). Virtually no long-term cooling trend  
 254 is apparent for the midwinter months of June-July.



255

256 Figure 5. The seasonal variability in (a) solar cycle and (b) long-term trend  
 257 coefficients derived using a 60 day sliding window (blue dots), and as monthly trends (grey  
 258 boxes) compared to the winter mean trends (red lines) derived for Fig. 3. The green lines  
 259 show the confidence limits (95%) for the trend coefficients.

260

#### 261 4.3 Aura/MLS trend comparison

262 For comparison with the Davis trend measurements, we use version v4.2 level 2  
 263 data from the Microwave Limb Sounder (MLS) instrument on the Earth Observing System  
 264 Aura satellite launched in July 2004 (Schwartz et al., 2008). Aura/MLS provides almost  
 265 complete global coverage ( $82^{\circ}$  S- $82^{\circ}$  N) of limb scanned vertical profiles ( $\sim 5$ - $100$  km) of



266 temperature and geopotential height derived from the thermal microwave emissions near  
267 the spectral lines 118 GHz O<sub>2</sub> and 234 GHz O<sup>18</sup>O. Previous comparisons of these data  
268 with MLS v2.2 temperatures were conducted by French and Mulligan, 2010.

269 Over-plotted in Fig. 3a (extending from 2005) are the equivalent Aura/MLS mean  
270 temperature anomalies computed by averaging all observations within 500 km of Davis,  
271 for months April to September (AMJJAS) over altitudes 83-88 km (blue line, obtained  
272 from a linear interpolation of Aura/MLS geopotential height profiles to geometric height  
273 in 1 km steps) and at the 0.00464 hPa (native Aura/MLS retrieval) pressure level (green  
274 line). The Aura/MLS data were selected according to the quality control recommendations  
275 described in Livesey et al. (2018). Approximately 60 samples/month are coincident within  
276 this range. We see close agreement considering that at these altitudes the vertical resolution  
277 (FWHM of the averaging kernel) of Aura/MLS is approximately 15 km (Schwartz et al.,  
278 2008). The Aura/MLS measurements closely follow the solar response, the magnitude and  
279 period of the quasi-quadrennial oscillation (QOO) and the underlying long-term linear  
280 trend. Statistically, the closest agreement is with the 0.00464 hPa pressure level and this is  
281 over-plotted on Fig. 3b corrected for the solar cycle response determined from the Davis  
282 OH measurements. The linear long-term trend fit for Aura/MLS over 14 years is -1.43  
283 K/decade (comparable to the -1.2 K/decade for the 24 years of Davis OH measurements)  
284 but clearly the underlying QOO variability has a significant effect on the fit.

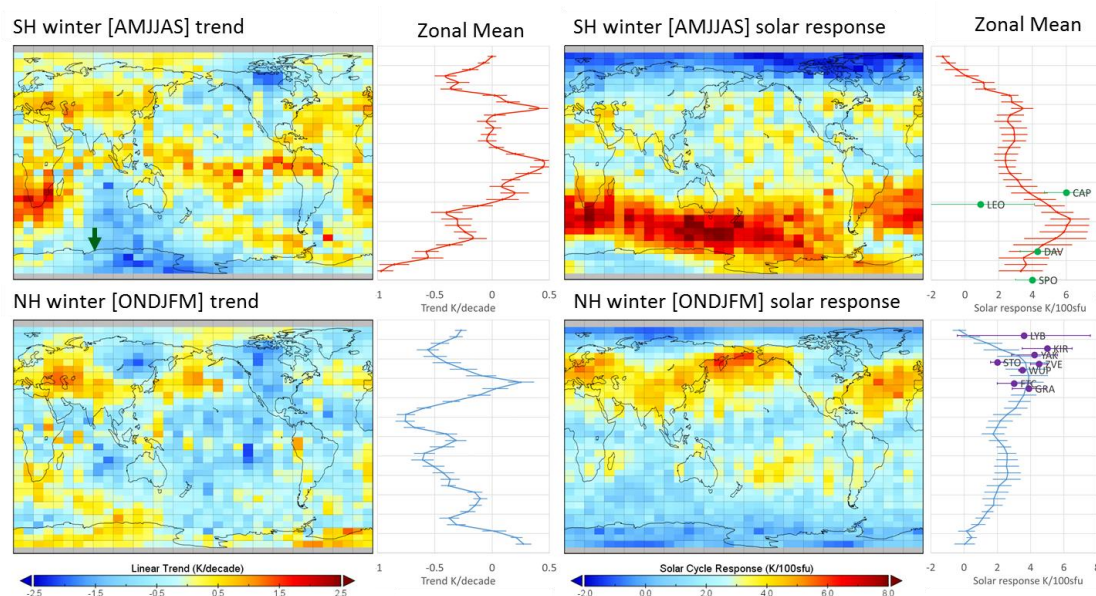
285 It is important to note that the winter mean residual trend coefficients in Fig. 3b are  
286 derived as a mean across 6-months of significantly varying solar and long-term responses.  
287 Nevertheless, the residual QOO signature remains readily apparent in the 60-day sliding  
288 window means through April to July [AMJJ] although somewhat breaking down in August  
289 to October [ASO].



290 We examine the QOO feature in more detail in the second part of this work (French,  
291 et al., 2019), but here, given the close agreement of Davis and Aura/MLS trends in Fig. 3b,  
292 we apply the same model fit procedure to derive Aura/MLS solar cycle and linear long-  
293 term trend coefficients to obtain a global picture of trends at the hydroxyl layer equivalent  
294 pressure level (0.0046 hPa). Figure 6 shows global trends determined by averaging  
295 Aura/MLS pressure level 0.0046 hPa temperature anomalies into a  $5^\circ \times 10^\circ$  (latitude  $\times$   
296 longitude) grid, over Southern Hemisphere (SH) winter months (AMJJAS; top panels)  
297 compared to Northern Hemisphere (NH) winter months (October-March; ONDJFM;  
298 bottom panels). Each grid box has been corrected for the solar cycle response determined  
299 from a linear regression of temperature to F10.7 over the 14 years of Aura/MLS  
300 measurements. The long-term linear trend (left-hand panels) and solar cycle response  
301 (right-hand panels), for each grid box, together with their corresponding zonal means are  
302 presented. The maps contain some interesting features; enhanced bands of solar activity  
303 response occur at mid-latitudes in both winter hemispheres although strongest in the SH  
304 (colour scales are the same for each hemisphere). Minima in sensitivity to solar forcing  
305 occur over the equator and the poles. Long-term trends over the Aura/MLS era are not  
306 globally uniform. While the global mean trend for the SH winter [AMJJAS] is -0.31  
307 K/decade, there are regions of warming, notably around the equator, southern Africa,  
308 Europe and the Atlantic ocean and strongest cooling over Antarctica and northern Canada.  
309 For the NH winter [ONDJFM] the global mean is -0.11 K/decade with generally global  
310 cooling, except for warming over Antarctica, Europe, southern Africa and the northern  
311 Pacific Ocean.



312



313

Figure 6. Global temperature trends and solar cycle responses, together with their corresponding zonal means determined from 14 years of MLS v4.2 pressure level 0.0046hPa (hydroxyl layer equivalent), averaged into  $5^\circ$  latitude  $\times$   $10^\circ$  longitude grid, and over southern hemisphere winter months (AMJJAS; top panels) compared to northern hemisphere winter months (ONDJFM; bottom panels). The linear trend and solar cycle response coefficients have been derived individually for each grid box from Aura/MLS over 14 years with no lag. The green arrow in panel 1 indicates the Aura/MLS comparison with Davis shown in Fig 1B. Solar response coefficients from other observers are indicated on the zonal solar response plots (see text for site information)

324

#### 4.4 Trend comparisons with other ground based observations

It is useful to compare these Aura/MLS derived solar response and trend coefficients with other observations, carefully bearing in mind that these observations may span different time intervals than available in the Aura/MLS measurement epoch. At Davis the solar cycle response (indicated by the green dot DAV in Fig. 6) determined over 24 years matches well with the zonal mean at  $68^\circ$  S determined from the Aura/MLS measurements. Davis appears to be on the poleward boundary of the strong band of solar



sensitivity ( $\sim 40\text{--}70^\circ \text{S}$ ) in the SH winter. The long-term trend at Davis is marked by the green arrow on the left-hand upper panel in Fig 6, and as we have seen from Fig. 3, agrees well with Aura/MLS.

Table 1 summarises the data-span, derived long term trend, and solar cycle coefficients from a collection of ground-based observers. Where new results are available these have been updated from Table 2 in French and Klekociuk (2011) and as compiled in Beig et al. (2008). The majority of these observations agree well with the Aura/MLS solar trend evaluated here, given it is a zonal mean response.

Site	Data Span	Trend K/decade	Solar response K/100sfu	Reference
Longyearbyen (LYB, $78^\circ\text{N}$ , $16^\circ\text{E}$ )	1983-2013	$-0.2 \pm 0.5$	$3.6 \pm 4.0$	Holmen et al. (2014)
Kiruna (KIR, $68^\circ\text{N}$ , $21^\circ\text{E}$ )	2003-2014	$-2.6 \pm 1.5$	$5.0 \pm 1.5$	Kim et al. (2017)
Yakutia (YAK, $63^\circ\text{N}$ , $129^\circ\text{E}$ )	1999-2013	Not Significant	$4.24 \pm 1.39$	Ammosov et al. (2014)
Stockholm (STO, $57^\circ\text{N}$ , $12^\circ\text{E}$ )	1991, 1993-1998	Not Determined	$2.0 \pm 0.4$	Espy et al. (2011)
Zvenigorod (ZVE, $56^\circ\text{N}$ , $37^\circ\text{E}$ )	2000-2016	$-0.07 \pm 0.03$	$4.5 \pm 0.5$	Perminov et al. (2018)
Wuppertal (WUP, $51^\circ\text{N}$ , $7^\circ\text{E}$ )	1988-2015	$-0.89 \pm 0.55$	$3.5 \pm 0.21$	Kalicinsky et al. (2016)
Fort Collins (FTC, $41^\circ\text{N}$ , $105^\circ\text{W}$ )	1990-2018	$-2.3 \pm 0.5$	$3.0 \pm 1.0$	Yuan et al. (2019 in press)
Granada (GRA, $37^\circ\text{N}$ , $3^\circ\text{W}$ )	2002-2015	$-0.6 \pm 2.0$	$3.9 \pm 0.1$	Garcia-Comas et al. (2017)
Cachoeira Paulista (CAP, $23^\circ\text{S}$ , $45^\circ\text{W}$ )	1987-2000	$-1.08 \pm 0.15$	$6 \pm 1.3$	Clemesha et al. (2005)
El Leoncito (LEO, $32^\circ\text{S}$ , $69^\circ\text{W}$ )	1998-2002	Not Determined	$0.92 \pm 3.2$	Scheer et al. (2005)
Davis (DAV, $68^\circ\text{S}$ , $78^\circ\text{E}$ )	1995-2018	$-1.20 \pm 0.51$	$4.30 \pm 1.02$	This Work
South Pole (SPO, $90^\circ\text{S}$ )	1994-2004	$0.1 \pm 0.2$	$4.0 \pm 1.0$	Azeem et al. (2007)

Table 1. A comparison of solar cycle response and temperature trend observations from the ground-based OH observer network with updates since 2011 where available.

As some observers have found, there is a significant question about a time delay in the OH layer temperature response to solar forcing via the various solar absorption mechanisms in the atmosphere. The major absorbers and altitude of solar extreme ultraviolet radiation are molecular oxygen (Schumann-Runge continuum, 80-130 km,



Schumann-Runge electronic and vibrational bands, 40-95 km, Herzberg continuum, below 50 km) and ozone (Hartley-Huggins bands, below 50 km).

We have previously found a lag of around 160 days (F10.7 leads temperature) is best fit to the linear model (French and Klekociuk, 2011), others find shorter: 80 days at Longyearbyen, Svalbard (Holmen et al. 2014), or larger lags: 25 months at Maimaga station, Yakutia (Ammosov et al. 2014; Reisin et al. 2014). Recalculating the long term trends for Aura/MLS assuming a uniform global solar response (as for Davis), or with a 160 day lag and zonal mean solar response (see supplementary material) does not significantly change the warming and cooling patterns shown in Fig. 2, but the lag does reduce the cooling trend (on average by 0.16 K/decade for the southern hemisphere (SH) winter and 0.11 K/decade for the northern hemisphere (NH) winter) and increases the fit error.

Beig (2011a, 2011b) in their reviews of long-term trends in the temperature of the mesosphere and lower thermosphere (MLT), highlight the difficulty of distinguishing between the anthropogenic and solar cycle influences. In their results, mesopause region temperature trends were found to be either slightly negative or zero. At that time, it was believed that the solar response becomes stronger with increasing latitude in the mesosphere with typical values in the range of a few degrees per 100 solar flux units in the lower part of the mesosphere but reaching 4-5 K/100 sfu near the mesopause. More recent studies using longer data sets (Ammosov et al. 2014; Holmen et al. 2014; Perminov et al. 2018) and satellite data (Tang et al. 2016) have reinforced that view.

Trend breaks began to appear in mesopause region temperatures in 2006 (Offermann et al. 2006), and these continue until now in certain locations (e.g., Jacobi et al., 2015; Kalicinsky et al., 2018; Yuan et al., 2019). These can be quite varied from site to site, ranging from -10 K/decade to +5 K/decade. Some of these estimates simply suffer from lack of observations (measurement spans less than a solar cycle). Few are longer than



376 2 solar cycles, but those of note are included in Table 1. OH temperature trend studies in  
377 the southern hemisphere are less common. Reid et al. (2017) report MLT-region nightglow  
378 intensities, temperatures and emission heights near Adelaide (35° S, 138° E), Australia.  
379 Five years (2001-2006) of spectrometer measurements using OH(6-2) and O<sub>2</sub>(0-1)  
380 temperature are compared with 2 years of Aura/MLS data and 4.5 years of SABER data.  
381 Venturini et al. (2018) report mesopause region temperature variability and its trend in  
382 southern Brazil (Santa Maria, 30° S, 54° W), based on SABER data over the period 2003-  
383 2014. Nath and Sridharan (2014) examined the response of the middle atmosphere  
384 temperature to variations in solar cycle, QBO and ENSO in the altitude range 20-100 km  
385 and 10-15° N latitude using monthly averaged zonal mean SABER observations for the  
386 years 2002-2012. They found cooling trends in most of the stratosphere and the mesosphere  
387 (40–90 km). In the mesosphere, they found the temperature response to the solar cycle to  
388 be increasingly positive above 40 km. The temperature response to ENSO was found to  
389 be negative in the middle stratosphere and positive in the lower and upper stratosphere,  
390 whereas it appeared largely negative in the height range 60–80 km and positive above 80  
391 km.

392



## 393 5. Discussion

### 394 5.1 Relationship between Davis trends and CO<sub>2</sub> change.

395 Our updated trend assessment over 24 years yields a cooling rate of  $-1.20 \pm 0.51$   
396 K/decade for the mean winter [D106-259] temperatures in the hydroxyl layer above Davis.  
397 A slightly greater rate of  $-1.32 \pm 0.45$  K/decade is derived if the full year [D040-310] of  
398 observations are included in the annual means. Over the same period, annual mean surface  
399 CO<sub>2</sub> volume mixing ratios (VMRs) increased from 360.82 ppm [1995] to 408.52 ppm  
400 [2018] (Mauna Loa values from Global Greenhouse Gas Reference Network  
401 [www.esrl.noaa.gov/gmd/ccgg/trends/](http://www.esrl.noaa.gov/gmd/ccgg/trends/)), an increase of 47.7 ppm or 13.2% (19.9 ppm per  
402 decade or 5.5% per decade). Qian et al. (2019) quote a CO<sub>2</sub> trend figure of 5.2%/decade  
403 (or 5.1 % if the seasonal variation is removed before the linear trend calculated) based on  
404 measurements made by TIMED/SABER from 2002-2015. If the primary factor for the  
405 observed temperature trend is considered to be CO<sub>2</sub> radiative cooling, a coefficient of -0.06  
406 K/ppmCO<sub>2</sub> or -0.22 K/%CO<sub>2</sub> is implied. This is approximately twice the value obtained  
407 by (Huang, 2018) (her Figure 2) who employed a linear scaling of the result of a doubling  
408 of CO<sub>2</sub> concentration by (Roble and Dickinson, 1989). A CO<sub>2</sub> increase of 26.5% from  
409 1960 to 2015 was accompanied by a temperature decrease of 1.4% at an altitude of 89.4  
410 km near Salt Lake city, Utah (18° N, 290° E).

411 CO<sub>2</sub> is well mixed through the lower atmosphere with a constant VMR up to about  
412 80 km. Above this height, diffusion and photolysis processes begin to have an effect,  
413 reducing the VMR (Garcia et al., 2014) but these processes vary with latitude and season  
414 (Rezac et al. 2015; López-Puertas et al., 2017).

415 Several studies of CO<sub>2</sub> VMR using profiles from the Atmosphere Chemistry  
416 Experiment Fourier Transform Spectrometer (ACE-FTS) and Sounding of the Atmosphere  
417 using Broadband Emission Radiometry (SABER) satellite instruments, reported



418 considerably larger rates of change of CO<sub>2</sub> in the upper atmosphere, increasing from about  
419 5% per decade at 80 km to 12% per decade at 110 km (Emmert et al., 2012; Garcia et al.,  
420 2016; Yue et al., 2015). However, more recent analysis of the ACE-FTS and SABER CO<sub>2</sub>  
421 data with different deseasonalizing procedures have shown an average rate of 5.5% per  
422 decade in the 80-110 km region, consistent with surface rates (Qian et al., 2019; Rezac et  
423 al., 2018).

424 In a recent summary of progress in trends in the upper atmosphere, Laštovička  
425 (2017) identified greenhouse gases, particularly CO<sub>2</sub> as the primary driver of long-term  
426 trends there. The important secondary trend drivers in the mesosphere and lower  
427 thermosphere (MLT) are stratospheric ozone, water vapour concentration and  
428 atmospheric dynamics. The overall effect of greenhouse gases at mesospheric altitudes is  
429 radiative cooling. Temperature trends are predominantly negative, and recent progress in  
430 understanding the magnitude of the cooling have arisen from confirmation and  
431 quantification of the role of ozone. In the mesopause region, about two thirds of the  
432 cooling is attributed to increases in CO<sub>2</sub> concentration and one third to changing  
433 concentration of ozone in the stratosphere (Lübken et al., 2013). Increases in water  
434 vapour concentration are considered a secondary but non-negligible effect particularly in  
435 the lower thermosphere (Akmaev et al. 2006). Trends in ozone vary as a function of both  
436 altitude and latitude, with positive trends dominating in the lower stratosphere and  
437 mesosphere.

438 Huang (2018) examined the influence of CO<sub>2</sub> increase, solar cycle variation and  
439 geomagnetic activity on airglow from 1960 to 2015 using two airglow chemistry dynamics  
440 models (OHCD – OH chemistry dynamics, and MACD – multiple airglow chemistry  
441 dynamics). As expected, the results showed that airglow intensity and peak volume  
442 emission rate (VER) are in phase and have a linear relationship with F10.7 values, whereas



CO<sub>2</sub> increase leads to a slowly decreasing trend in OH(8-3) airglow intensity. OH(8-3) peak altitudes of the VER are unaffected by increases in CO<sub>2</sub> concentration, and are only slightly affected by the F10.7 cycle, with slightly lower peak altitudes when F10.7 is <100 SFU. Surprisingly, OH VER peak heights showed a significant inverse relationship with geomagnetic activity as measured by the Ap index. We find no significant correlation of the *T*-residual from Davis with the Ap index for the months of AMJJAS.

Lübken et al. (2013) present the results of trend studies in the mesosphere in the period 1961-2009 from the Leibniz-Institute Middle Atmosphere (LIMA) chemistry-transport model which is driven with European Centre for Medium-Range Weather Forecasts (ECMWF) reanalysis below 40 km, and observed variations of CO<sub>2</sub> and O<sub>3</sub>. They find that CO<sub>2</sub> is the main driver of temperature change in the mesosphere, with O<sub>3</sub> contributing approximately one third to the trend. Linear temperature trends were found to vary substantially depending on the time period chosen primarily due to the influence of the complicated temporal variation of ozone. The trend effect of dynamics was found to be very slightly negative in the mesosphere, but very small compared with the radiatively induced trends. At the mesopause, the trend due to dynamics was positive and significantly larger (~1 K/decade). These results were found to be in good agreement with observations from lidars, Stratospheric Sounding Units (SSU) (Randall et al., 2009) and radio reflection heights which have decreased by more than 1 km in the last 50 years due to shrinking in the stratosphere/lower mesosphere caused by cooling. Figure 3 of (Lübken et al., 2013) show a monotonically increasing trend on CO<sub>2</sub> compared with a much more complicated temporal ozone variation (essentially constant until 1980, a rapid decrease from 1980-1995, followed by an increase since then).

A recent paper by Hervig et al. (2019) report on the absence of a solar signal correlated response in polar mesospheric clouds (PMCs) in the summer mesopause



468 following 2002. PMCs are controlled by temperature and water vapour. At solar maximum,  
469 temperatures are expected to be higher and water vapour lower, thereby leading to less  
470 PMCs at solar maximum. This anti-correlation was evident in satellite data until 2002, but  
471 has been absent since then. The main cause for the diminished solar cycle in PMCs at 68°  
472 N and 68° S appears to be the dramatic suppression of the solar cycle response in water  
473 vapour. The solar cycle response of temperature also decreases after 2002, but has a much  
474 lower effect on PMCs than the water vapour.

475 The Whole Atmosphere Community Climate Model (WACCM) extended into  
476 thermosphere (upper boundary ~700 km) (WACCM-X) was used by Qian et al. (2019)  
477 (with the lower atmosphere constrained by reanalysis data) to investigate temperature  
478 trends and the effect of solar irradiance on temperature trends on the mesosphere during  
479 the period 1980-2014. The overall temperature trend in the mesopause region at 85 km  
480 was statistically insignificant at  $-0.46 \pm 0.60$  K/decade. Solar irradiance effects on the  
481 global average temperature are positive and decrease monotonically with decreasing  
482 altitude from a value of ~3 K/100 sfu in the lower thermosphere to ~1 K/100 SFU at 55  
483 km. This is readily explained by the decreasing external energy from the Sun with reducing  
484 altitude. A monthly mean global average trend of 2.46 K/100 sfu is quoted for the  
485 mesopause near 85 km. The mesosphere is affected by solar irradiance directly from local  
486 heating through absorption of radiation, and indirectly through dynamics by its effects on  
487 the geostrophic winds which control the upward propagation of gravity waves and  
488 planetary waves generated in the troposphere. Zonal mean temperatures show significant  
489 variability as a function of altitude, latitude and season. Qian et al. (2019) provide globally  
490 averaged temperature trend values as a function of altitude and latitude for each month  
491 some of which are statistically significant. Solar cycle effects on temperature are in  
492 reasonable agreement with the OH(6-2) temperatures shown in Figure 5 with positive



493 values ranging from ~3-5 K/100 sfu, the largest values occurring in July and October. The  
494 long-term trend is predominantly negative with values in the range -1 to -3 K/decade with  
495 the largest cooling occurring in March and September at the latitude and altitude of the OH  
496 temperatures measured at Davis Station. WACCM-X shows slightly positive trend values  
497 in the months of February, November and December at Davis Station, but OH(6-2)  
498 temperature data are not available in these months. The September maximum in cooling is  
499 in reasonable agreement with the Davis measurements shown in Figure 5 of this work.

500 More recent results from Garcia et al. (2019) using WACCMv4 free-running  
501 (coupled ocean) simulations for the period 1955-2100 using IPCC RCP 6.0 attribute the  
502 changes in the trends of the temperature profile to monotonic increases in CO<sub>2</sub>  
503 concentration together with a decrease in O<sub>3</sub> until 1995 followed by subsequent increase.  
504 Garcia et al. (2019) assign half of the stratopause negative temperature trend to ozone  
505 depleting substances. At the mesopause, the global mean trend in temperature is  
506 approximately -0.6 K/decade. Solar cycle signals at the mesopause are in the range 2-3  
507 K/100 sfu with slightly higher values in the southern polar cap. Very large seasonal trends  
508 in temperature at all altitudes are associated with the development of the Antarctic ozone  
509 hole. Trends are largest in the November-December period, and teleconnections are made  
510 with the upper mesosphere via GW filtering by the zonal wind anomaly in the southern  
511 polar cap

512

## 513 5.2 Trend breaks.

514 When analysing long-term trends, several authors (Lübken et al., 2013; Qian et al.,  
515 2019) emphasise the importance of specifying the length of the time period, as well as the  
516 beginning and end of the period, because trend drivers can be different for different periods  
517 (e.g., Yuan et al., 2019). Yuan et al. (2019) report long-term trends of the nocturnal



mesopause temperature and altitude from LIDAR observations at mid-latitude (41-42° N, 105-112° W) in the period 1990-2018. They divided their observations into two categories, the high mesopause (HM) above 97 km during the non-summer months, mainly formed by radiative cooling, and the low mesopause (LM) below 92 km during the non-winter months generated by mostly by adiabatic cooling. This idea of the mesopause at two different altitudes is well established (e.g., von Zahn et al., 1996; Xu et al., 2007; Thulasiraman and Nee, 2002). Although Yuan et al. (2019) obtained a cooling trend of more than 2K/decade in the mesopause temperature along with a decreasing trend in mesopause height since 1990, the temperature trend is statistically insignificant since 2000.

Trend breaks have been reported at other mid-latitude stations (Offermann et al., 2006) where a discontinuity was found in the overall trend in the year 2001/2002. Using some of the same data as Offermann et al. (2006), Kalicinsky et al. (2016) reported a trend break in the middle of 2008. Before the break point, there is a clear negative trend reported to be  $-2.4 \pm 0.7$  K/decade, whereas after 2008, a large positive trend of  $6.4 \pm 3.3$  K/decade is deciphered. Two possible explanations are suggested for the trend break: the first is that it is the result of a combination of the solar cycle and a long period oscillation such as the 22-year Hale cycle of the Sun. A second possible explanation of the very substantial change in the trend at 2008 is a combination of the solar flux with a sensitivity of  $4.1 \pm 0.8$  K /100 SFU together with a long period oscillation 24-26 years with an amplitude of about 2K. Kalicinsky et al. (2018) find support for this idea in the identification of a quasi-decadal oscillation in the summer mesopause over Western Europe in plasma scale height observations (near 80 km altitude) which are in anti-correlation with the potential oscillation in temperature from OH\* measurements. The anti-correlation in the two data sets is explained on the basis of the fact that they originate below (plasma scale height data) and above (OH\* temperature data) the temperature minimum in the mesopause region in



543 summer. Jacobi et al. (2015) find that the long-term behavior of both meridional and zonal  
544 winds at 90-95 km in northern mid-latitude stations exhibit trend breaks in summer near  
545 1999, although the winter data are well described by a single linear trend over the years  
546 1980- 2015. We find no obvious sign of a discontinuity in the trend obtained in the Davis  
547 data.

548

### 549 5.3 Effect of changes in the OH\*-layer height

550 There is widespread acceptance that cooling of the middle atmosphere due to  
551 increases in CO<sub>2</sub> concentration has resulted in shrinking of the middle atmosphere (e.g.,  
552 (Grygalashvyly et al., 2014; Sonnemann et al., 2015). This does raise the question  
553 however of whether the OH\* layer is fixed to a constant pressure level rather than a  
554 constant altitude. There are mixed reports on this topic. In a long-term study of the  
555 effects of chemistry, greenhouse gases, and the solar modulation on OH\* layer trends  
556 using the Leibniz Institute Middle Atmosphere (LIMA) chemistry-transport model  
557 covering the period 1969 to 2009, Grygalashvyly et al. (2014) reported a downward shift  
558 in the OH\*-layer by about 0.3 km/decade in all seasons due to shrinking of the middle  
559 atmosphere resulting from radiative cooling by increasing CO<sub>2</sub> concentrations. Wüst et  
560 al. (2017) report a descent in the mean altitude of the OH\* layer of 0.02 km/ year from 14  
561 years of SABER data (2002-2015) in the alpine region of southern Europe (44–48° N, 6–  
562 12° E). They refer to a paper by Bremer and Peters (2008) which reports low frequency  
563 reflection heights (ca. 80-83 km) between 1959 and 2006 and derive a figure of 0.032  
564 km/year.

565 Sivakandan et al. (2016) have published a long-term variation paper on OH peak  
566 emission altitude and volume emission rate over Indian low latitudes using SABER data.



567 A weak decreasing trend of 19.56 m/year was reported for the peak emission altitude of  
568 the night-time OH\*-layer.

569  
570 A vertical shift of the OH\* layer either upward or downward gives rise to a change  
571 in the emission weighted temperature which is measured by ground-based optical  
572 instruments (French and Mulligan, 2010; von Savigny, 2015). Von Savigny (2015)  
573 reported no apparent trend or solar cycle in OH emission altitude at the local time of the  
574 SCIAMACHY nighttime observations in the period 2003-2011. However, Teiser and von  
575 Savigny (2017) found evidence of an 11-year solar cycle in the vertically integrated  
576 emission rate and in the centroid emission altitude of both the OH(3-1) and OH(6-2) bands  
577 in SCIAMACHY data. Gao et al. (2016) found no evidence that the OH\* peak heights are  
578 affected by solar cycle in 13 years of TIMED/SABER data, and deduced that the solar  
579 cycle variation of temperature obtained from ground-based OH nightglow observations  
580 were essentially immune from the OH emission altitude variations. Huang (2018) found  
581 no systematic response of airglow O(<sup>1</sup>S) green line, O<sub>2</sub>(0,1), or OH(8-3)) VER peak heights  
582 with the F10.7 solar cycle using two airglow models OHCD and MACD-90. The Huang  
583 (2018) result is supported by Gao et al. (2016) using TIMED/SABER data and by von  
584 Savigny (2015) using SCIAMACHY data. These confirmations of the remarkable long-  
585 term stability of the peak altitude of the OH\*-layer in an atmosphere with increasing CO<sub>2</sub>  
586 concentration and changing solar radiation are essential for the use of long-term studies of  
587 mesopause region temperatures derived from ground-based OH\* optical measurements.

588 We have examined the altitude of the OH\* layer during the period 2002-2018  
589 using the OH-B channel volume mission rate (VER) from TIMED/SABER (version 2.0)  
590 sensitive in the wavelength range 1.56-1.72 μm, which includes mostly the OH(4-2) and  
591 OH(5-3) bands. All VER altitude profiles between day 105 and day 259 that satisfied the  
592 selection criteria (tangent point within 500 km of Davis and solar zenith angle > 97°),



employed by French and Mulligan (2010) were used to determine the altitude of the layer. The altitude of the peak was obtained from a Gaussian profile fitted to the VER profile (for more details, see French and Mulligan, 2010). The slope of the best fit line to the winter annual average peak altitude was  $-0.02 \pm 0.02$  km/ year as shown in Figure 7, i.e., no significant change in altitude of the layer over the period in agreement with the result of Gao et al. (2016).

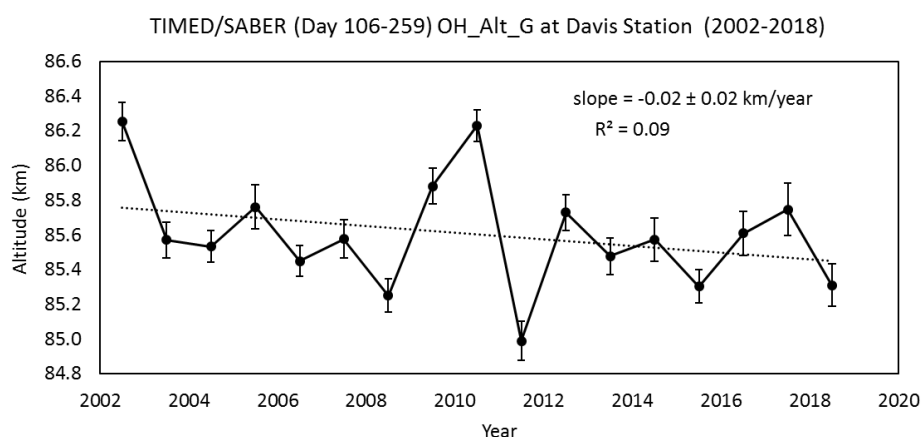


Figure 7. The trend in the mean winter OH layer altitude, derived from TIMED/SABER (version 2.0) OH-B channel volume emission rate. The slope of the best fit line is  $-0.02 \pm 0.02$  km/year, i.e., no significant change in altitude of the layer over this interval.

#### 5.4 Global solar cycle and linear trends

The trend measured at Davis is well matched with the result from Aura/MLS over 14 years for the southern hemisphere (SH) winter months (AMJJAS) at the 0.0046 hPa level. Clearly though, applying the same analysis to the global temperature field reveals that trends are not globally uniform (Fig 6). In the SH winter the most significant cooling trends are seen over the southern polar cap and northern Canada, with warming trends over southern Africa, around the equator and over Europe and Russia. NH winter cooling trends



612 are strongest over eastern Russia and North America, but warming trends remain over  
613 Europe.

614 There are a number of limitations and assumptions made for these derived trends:

615 i) there are only 14 years from which to extract a solar cycle component, ii) a solar cycle  
616 component is computed for each grid box. The zonal means calculated are generally within  
617 2 K/100 sfu of other reported solar response coefficients, but there is a strong latitudinal  
618 and seasonal dependence (strongest solar flux response in mid-latitude winter hemisphere  
619 – near zero response in high latitude summer), iii) we have assumed no lag between solar  
620 flux variations and the temperature response, whereas previous work for the Davis response  
621 for example indicates a ~160 day lag is optimal (French and Klekociuk, 2011) and iv) for  
622 comparison with other hydroxyl temperature long-term trends we assume the global OH  
623 layer height is well matched with the Aura/MLS 0.0046 hPa level.

624 To address uncertainties about the solar response coefficient we have recalculated  
625 the global trends assuming a fixed response for each grid box (4.2 K/100 sfu derived from  
626 the Davis observations) and also as zonal means but for a lag of 160 days (F10.7 leads T)  
627 as previously found for Davis. These plots are available in the supplementary material and  
628 show that, by and large, the warming and cooling patterns observed in Figure 6 do not  
629 change significantly for the different solar cycle components.

630 While the WACCM-X results presented by Qian et al. (2019) are in reasonable  
631 agreement with the OH temperature behaviour measured at Davis Station, the zonally  
632 averaged pattern of solar cycle response and linear trend obtained from WACCM-X differs  
633 considerably from that obtained from an analysis of the Aura/MLS data at the 0.00464 hPa  
634 level shown in Figure 6. In the Aura/MLS results, the solar response in both hemispheres  
635 in winter show a great deal more variation as a function of latitude than is evident in the  
636 WACCM-X results at 87 km (Figure 4 of Qian et al., 2019). The zonally averaged



637 Aura/MLS pattern shows maxima in southern mid-latitudes in the Southern Hemisphere  
638 (SH) winter, while the maximum is in northern mid-latitudes in the Northern Hemisphere  
639 (NH) winter. The solar cycle response is essentially zero at 82° north and south during the  
640 NH winter months, but it is of the order of 3 K/decade at 82° south in SH winter. The  
641 southern hemisphere winter months have the largest variation with a pronounced maximum  
642 in the latitude range ~10° S to 40° S. (The maximum also shows longitudinal structure  
643 with a much broader maximum between 90° east and 90° west which is centred at higher  
644 southern latitudes.)

645 The WACCM-X long term trend is predominantly negative or zero at the altitude  
646 of the OH layer (87 km) at all latitudes and in all months apart from February, November  
647 and December, when a positive trend of up to ~3 K/decade is present at high southern  
648 latitudes. Aura/MLS results also show a predominantly slight negative trend ~0.5-1  
649 K/decade, except at the equator, and at mid-latitudes in the SH winter months.

650 Solomon et al. (2018) simulated the anthropogenic global change through the entire  
651 atmosphere using WACCM-X in a free-running mode (i.e., lower atmosphere below 50  
652 km not constrained by ECMWF reanalysis data) using constant low solar activity  
653 conditions. They find substantial cooling in the mesosphere of the order of -1 K/decade,  
654 increasing to -2.8K/decade in the thermosphere. Temperature decreases were small near  
655 the mesopause compared with the variation in the annual mean thus making trends there  
656 somewhat uncertain. Solomon et al. (2018) conclude that inconsistent observational results  
657 in the mesopause region, together with little or no global mean trends is due to the  
658 dominance of dynamical processes in controlling mesopause temperature, which exhibits  
659 significant interannual variability, even without variable solar forcing.

660 The SABER dataset (2002-2015) was used by Tang et al. (2016) to study the  
661 response of the cold-point temperature of the mesopause (T-CPM) to solar activity. The



662 results showed that the T-CPM is significantly correlated to solar activity at all latitudes,  
663 and the solar response becomes stronger with increasing latitude. The solar-cycle  
664 dependence of the mesopause cold point temperature (T-CPM) is due to the relative  
665 importance of CO<sub>2</sub> and NO infrared cooling (Tang et al., 2016). NO density at solar max  
666 is about three times that at solar minimum. Consequently, CO<sub>2</sub> cooling is relatively less  
667 important at solar maximum, but is the dominant cooling mechanism during solar  
668 minimum.

669 Values of the solar response of T-CPM reported by Tang et al. (2016) increased  
670 from  $2.82 \pm 0.73$  K/100 sfu at 0-10° S to  $6.35 \pm 1.16$  K/100 sfu at 60-70° S. Correlation  
671 coefficients of mesopause temperature with F10.7 cm solar irradiance data were higher for  
672 mid-latitudes ( $> 0.9$ ) than at the equator ( $\sim 0.7$ ) and at higher latitude. The value found for  
673 70° S ( $\sim 0.8$ ) is consistent with the correlation coefficient obtained for the OH\*  
674 temperatures (Figure 1(a)  $(0.584)^{1/2} \sim 0.76$ ) obtained in this work. At low latitudes, one  
675 would expect the QBO and ENSO to be significant factors there (see e.g., Nath and  
676 Sridharan, 2014), but at high latitudes, gravity wave activity is a candidate for the missing  
677 variance. Inter-annual variations of GWs at high latitudes are correlated with the strength  
678 of the polar vortex. A stronger polar vortex filters out more eastward propagating GWs,  
679 thus leading to more westward GW drag, which drives stronger meridional circulation  
680 (Karlsson and Shepherd, 2018).

681 Although the altitude of the cold point changes with season (e.g., Yuan et al., 2019)  
682 it tends to be higher than the centroid of the OH\* layer, the global solar response value  
683 obtained for T-CPM ( $4.89 \pm 0.67$  K/100 SFU) is in good agreement with the solar response  
684 coefficient derived from ground-based OH\* observations.

685 The solar response of the T-CPM in Tang et al. (2016) shows some significant  
686 differences from the results in Figure 6 (zonal mean cycle from Aura/MLS) of this work.



687 The solar response of the T-CPM increases more or less monotonically with latitude,  
688 whereas the solar response registered by Aura/MLS maximises at higher mid-latitudes. Of  
689 course the height of the T-CPM is some 7 km higher on average as indicated in Figure 9  
690 (b) of Tang et al. (2016).

691 Several authors (Perminov et al., 2014; Pertsev and Perminov, 2008) have reported  
692 that winter OH\* temperatures are more sensitive to the solar flux variation than summer  
693 temperatures. This agrees with the Aura/MLS variation shown in Figure 6.

694 As a final comment on the global trends, it is noted that the largest errors in the  
695 linear trend fit for the SH winter occur coincident with the regions positive or negatively  
696 correlated with the QQO (cf. figure 3. i.e., eastern Antarctic polar cap, southern Pacific and  
697 southern Indian oceans). This is understandable if there is a significant QQO signal  
698 superposed on the underlying long-term linear trend.

699

## 700 6. Summary and Conclusions

701 We provide updates for the long-term trend and solar cycle response derived from  
702 24 years of spectrometer observations of hydroxyl airglow at Davis Research Station,  
703 Antarctica (68° S, 78° E). A cooling trend in the mean winter temperatures [D106-259] of  
704  $-1.20 \pm 0.51$  K/decade (95% confidence limits  $-0.14$  K/decade  $< L < -2.26$  K/decade) is  
705 obtained coupled with a solar cycle response coefficient of  $4.30 \pm 1.02$  K/100sfu (95%  
706 confidence limits  $2.2$  K/100sfu  $< S < 6.4$  K/100sfu). The observed cooling is consistent  
707 with radiative cooling due to increasing CO<sub>2</sub> concentrations and a rate of  $-0.06$  K/ppmCO<sub>2</sub>  
708 or  $-0.22$  K/%CO<sub>2</sub> is implied (ignoring possible contributions of stratospheric ozone change  
709 to the trend). A significant note is that a new record low winter-mean temperature was set  
710 for the Davis measurements in 2018, with a value of 198.3 K, which is 1.7 K below the



711 previous minimum recorded in 2009 (200.0 K). An examination of the seasonal variation  
712 in the trend fit parameters reveals very little (no significant) long-term trend occurs over  
713 the 2 midwinter months of June and July, but 95% significant trends of -1.5 to -2.6  
714 K/decade during the April-May and August-October intervals. From examination of  
715 TIMED/SABER VER profiles we see no evidence that the trend results obtained can be  
716 significantly attributed to a change in the height of the OH layer.

717 We do not see evidence of a trend break or a change in the nature of the underlying  
718 trend after accounting for the solar cycle response in the Davis OH temperatures, however,  
719 this simple solar-cycle and linear trend model fit accounts for only 58% of the temperature  
720 variability. The remaining variability reveals evidence of a temperature oscillation on a  
721 quasi-quadrennial (~4 year period) timescale.

722 We compare our observations with Aura/MLS version v4.2 level 2 data over the  
723 last 14 years when these satellite data are available and find close agreement (a best fit)  
724 with the 0.00464 hPa (native Aura/MLS retrieval) pressure level values. The solar cycle  
725 response, long-term trend and underlying QQO residuals are consistent with the Davis  
726 observations. Consequently, we derive global maps of Aura/MLS trend and solar response  
727 coefficients for the SH and NH winter periods to compare with other observers and models.  
728 Significant patterns for the zonally averaged solar cycle response are maxima in southern  
729 mid-latitudes in the Southern Hemisphere (SH) winter and in northern mid-latitudes in the  
730 Northern Hemisphere (NH) winter. Long term trends are a predominantly slight negative  
731 (~0.5-1 K/decade), except at the equator, and at mid-latitudes in the SH winter months.  
732 Comparisons are also made with the WACCM-X model and mesopause cold point  
733 temperature versus solar activity study using TIMED/SABER data of Tang et al. (2016),  
734 both of which reveal significant differences in the zonally averaged patterns of solar cycle  
735 response and linear trend compared to the Aura/MLS data at 0.00464 hPa.



736 Further analysis using the datasets described here are undertaken to examine the  
737 residual QQO signal that this analysis has revealed. A second part of this paper “Analysis  
738 of 24 years of mesopause region OH rotational temperature observations at Davis,  
739 Antarctica. Part 2: Evidence of a quasi-quadrennial oscillation (QQO) in the polar  
740 mesosphere.” concerns this observation.

741

## 742 Data Availability

743 All Davis hydroxyl rotational data described in this manuscript are available through the  
744 Australian Antarctic Data Centre website (ref project AAS4157) via the following link  
745 [https://data.aad.gov.au/metadata/records/Davis\\_OH\\_airglow](https://data.aad.gov.au/metadata/records/Davis_OH_airglow) . The satellite data used in  
746 this paper were obtained from the Aura/MLS data centre (see <https://mls.jpl.nasa.gov>), the  
747 SABER data centre (see <http://saber.gats-inc.com/data.php>) and are publicly available.

748

## 749 Author Contribution

750 WJRF managed data collection, performed data analysis, prepared manuscript with  
751 contributions from all co-authors  
752 FJM analysis of SABER data, manuscript editing, figures, references  
753 ARK analysis of Aura/MLS satellite data, manuscript editing.

754

## 755 Competing Interests

756 The authors declare that they have no conflict of interest.

757



## 758 Acknowledgements

759 The authors thank the dedicated work of the Davis optical physicists and  
760 engineers over many years in the collection of airglow data and calibration of  
761 instruments. This work is supported by the Australian Antarctic Science Advisory  
762 Council (project AAS 4157).

763 The satellite data used in this paper were obtained from the Aura/MLS data centre  
764 (see <https://mls.jpl.nasa.gov>), the SABER data centre (see [http://saber.gats-](http://saber.gats-inc.com/data.php)  
765 [inc.com/data.php](http://saber.gats-inc.com/data.php)) and are publicly available. We thank those teams and acknowledge the  
766 use of these data sets.

767 This work contributes to the understanding of mesospheric change processes  
768 coordinated through the Network for Detection of Mesospheric Change (see  
769 <https://ndmc.dlr.de/>)

## 770 References

- 771 Akmaev, R. A., Fomichev, V. I. and Zhu, X.: Impact of middle-atmospheric composition  
772 changes on greenhouse cooling in the upper atmosphere, *J. Atmos. Solar-Terrestrial*  
773 *Phys.*, 68(17), 1879–1889, doi:10.1016/j.jastp.2006.03.008, 2006.
- 774 Ammosov, P., Gavriljeva, G., Ammosova, A. and Koltovskoi, I.: Response of the  
775 mesopause temperatures to solar activity over Yakutia in 1999–2013, *Adv. Sp. Res.*,  
776 54(12), 2518–2524, doi:10.1016/J.ASR.2014.06.007, 2014.
- 777 Azeem, S. M. I., Sivjee, G. G., Won, Y.-I. and Mutiso, C.: Solar cycle signature and  
778 secular long-term trend in OH airglow temperature observations at South Pole,  
779 *Antarctica, J. Geophys. Res. Sp. Phys.*, 112(A1), n/a-n/a, doi:10.1029/2005JA011475,  
780 2007.
- 781 Beig, G.: Trends in the mesopause region temperature and our present understanding-an



- 782 update, *Phys. Chem. Earth*, 31(1–3), 3–9, doi:10.1016/j.pce.2005.03.007, 2006.
- 783 Beig, G.: Long-term trends in the temperature of the mesosphere/lower thermosphere  
 784 region: 1. Anthropogenic influences, *J. Geophys. Res. Sp. Phys.*, 116(A2), n/a–n/a,  
 785 doi:10.1029/2011JA016646, 2011a.
- 786 Beig, G.: Long-term trends in the temperature of the mesosphere/lower thermosphere  
 787 region: 2. Solar response, *J. Geophys. Res. Sp. Phys.*, 116(A2), n/a–n/a,  
 788 doi:10.1029/2011JA016766, 2011b.
- 789 Beig, G., Keckhut, P., Lowe, R. P., Roble, R. G., Mlynczak, M. G., Scheer, J., Fomichev,  
 790 V. I., Offermann, D., French, W. J. R., Shepherd, M. G., Semenov, A. I., Remsberg, E.  
 791 E., She, C. Y., Lübken, F. J., Bremer, J., Clemesha, B. R., Stegman, J., Sigernes, F. and  
 792 Fadnavis, S.: Review of mesospheric temperature trends, *Rev. Geophys.*, 41(4),  
 793 doi:10.1029/2002RG000121, 2003.
- 794 Beig, G., Scheer, J., Mlynczak, M. G. and Keckhut, P.: Overview of the temperature  
 795 response in the mesosphere and lower thermosphere to solar activity, *Rev. Geophys.*,  
 796 46(3), doi:10.1029/2007RG000236, 2008.
- 797 Bengtsson, L., Hagemann, S. and Hodges, K. I.: Can climate trends be calculated from  
 798 reanalysis data?, *J. Geophys. Res.*, 109(D11), D11111, doi:10.1029/2004JD004536,  
 799 2004.
- 800 Bremer, J. and Peters, D.: Influence of stratospheric ozone changes on long-term trends in  
 801 the meso- and lower thermosphere, *J. Atmos. Sol. Terr. Phys.*, 70, 1473–1481, 2008.
- 802 Brooke, J. S. A., Bernath, P. F., Western, C. M., Sneden, C., Afşar, M., Li, G. and  
 803 Gordon, I. E.: Line strengths of rovibrational and rotational transitions in the  $X^2\Pi$   
 804 ground state of OH, *J. Quant. Spectrosc. Radiat. Transf.*, 168, 142–157,  
 805 doi:10.1016/j.jqsrt.2015.07.021, 2016.
- 806 Burns, G. B., Kawahara, T. D., French, W. J. R., Nomura, A. and Klekociuk, A. R.: A



- 807 comparison of hydroxyl rotational temperatures from Davis (69°S, 78°E) with sodium
- 808 lidar temperatures from Syowa (69°S, 39°E), *Geophys. Res. Lett.*, 30(1),
- 809 doi:10.1029/2002GL016413, 2003.
- 810 Clemesha, B., Takahashi, H., Simonich, D., Gobbi, D. and Batista, P.: Experimental
- 811 evidence for solar cycle and long-term change in the low-latitude MLT region, *J. Atmos.*
- 812 *Solar-Terrestrial Phys.*, 67(1–2), 191–196, doi:10.1016/j.jastp.2004.07.027, 2005.
- 813 Emmert, J. T., Stevens, M. H., Bernath, P. F., Drob, D. P. and Boone, C. D.:
- 814 Observations of increasing carbon dioxide concentration in Earth's thermosphere, *Nat.*
- 815 *Geosci.*, 5(12), 868–871, doi:10.1038/ngeo1626, 2012.
- 816 Espy, P. J., Ochoa Fernández, S., Forkman, P., Murtagh, D. and Stegman, J.: The role of
- 817 the QBO in the inter-hemispheric coupling of summer mesospheric temperatures, *Atmos.*
- 818 *Chem. Phys.*, 11(2), 495–502, doi:10.5194/acp-11-495-2011, 2011.
- 819 Fomichev, V. I., Jonsson, A. I., de Grandpré, J., Beagley, S. R., McLandress, C.,
- 820 Semeniuk, K. and Shepherd, T. G.: Response of the middle atmosphere to CO<sub>2</sub> doubling:
- 821 Results from the Canadian middle atmosphere model, *J. Clim.*, 20(7), 1121–1144,
- 822 doi:10.1175/JCLI4030.1, 2007.
- 823 French, W.J.R.; Klekociuk, A.R.; Mulligan, F. J.: Analysis of 24 years of mesopause
- 824 region OH rotational temperature observations at Davis, Antarctica. Part 2: Evidence of a
- 825 quasi-quadrennial oscillation (QO) in the polar mesosphere., *Atmos. Chem. Phys.*, 2019.
- 826 French, W. J. R. and Burns, G. B.: The influence of large-scale oscillations on long-term
- 827 trend assessment in hydroxyl temperatures over Davis, Antarctica, *J. Atmos. Solar-*
- 828 *Terrestrial Phys.*, 66(6–9), 493–506, doi:10.1016/j.jastp.2004.01.027, 2004.
- 829 French, W. J. R. and Klekociuk, A. R.: Long-term trends in Antarctic winter hydroxyl
- 830 temperatures, *J. Geophys. Res.*, 116(D4), D00P09, doi:10.1029/2011JD015731, 2011.
- 831 French, W. J. R. and Mulligan, F. J.: Stability of temperatures from TIMED/SABER



832 v1.07 (2002–2009) and Aura/MLS v2.2 (2004–2009) compared with OH(6-2)  
 833 temperatures observed at Davis Station, Antarctica, *Atmos. Chem. Phys.*, 10(23), 11439–  
 834 11446, doi:10.5194/acp-10-11439-2010, 2010.

835 French, W. J. R., Burns, G. B., Finlayson, K., Greet, P. A., Lowe, R. P. and Williams, P.  
 836 F. B.: Hydroxyl (6–2) airglow emission intensity ratios for rotational temperature  
 837 determination, *Ann. Geophys.*, 18(10), 1293–1303, doi:10.1007/s00585-000-1293-2,  
 838 2000.

839 Gao, H., Xu, J. and Chen, G.: The responses of the nightglow emissions observed by the  
 840 TIMED/SABER satellite to solar radiation, *J. Geophys. Res. Sp. Phys.*, 121(2), 1627–  
 841 1642, doi:10.1002/2015JA021624, 2016.

842 García-Comas, M., López-González, M. J., González-Galindo, F., de la Rosa, J. L.,  
 843 López-Puertas, M., Shepherd, M. G. and Shepherd, G. G.: Mesospheric OH layer altitude  
 844 at midlatitudes: variability over the Sierra Nevada Observatory in Granada, Spain (37° N,  
 845 3° W), *Ann. Geophys.*, 35(5), 1151–1164, doi:10.5194/angeo-35-1151-2017, 2017.

846 Garcia, R. R., López-Puertas, M., Funke, B., Marsh, D. R., Kinnison, D. E., Smith, A. K.  
 847 and González-Galindo, F.: On the distribution of CO<sub>2</sub> and CO in the mesosphere and  
 848 lower thermosphere, *J. Geophys. Res.*, 119(9), 5700–5718, doi:10.1002/2013JD021208,  
 849 2014.

850 Garcia, R. R., López-Puertas, M., Funke, B., Kinnison, D. E., Marsh, D. R. and Qian, L.:  
 851 On the secular trend of CO<sub>x</sub> and CO<sub>2</sub> in the lower thermosphere, *J. Geophys. Res.*,  
 852 121(7), 3634–3644, doi:10.1002/2015JD024553, 2016.

853 Garcia, R. R., Yue, J. and Russell, J. M.: Middle atmosphere temperature trends in the 20  
 854 th and 21 st centuries simulated with the Whole Atmosphere Community Climate Model  
 855 (WACCM) , *J. Geophys. Res. Sp. Phys.*, doi:10.1029/2019ja026909, 2019.

856 Greet, P. A., French, W. J. R., Burns, G. B., Williams, P. F. B., Lowe, R. P. and



- 857 Finlayson, K.: OH(6-2) spectra and rotational temperature measurements at Davis,
- 858 Antarctica, *Ann. Geophys.*, 16(1), 77–89, doi:10.1007/s00585-997-0077-3, 1997.
- 859 Grygalashvyly, M., Sonnemann, G. R., Lübken, F. J., Hartogh, P. and Berger, U.:
- 860 Hydroxyl layer: Mean state and trends at midlatitudes, *J. Geophys. Res. Atmos.*, 119(21),
- 861 12,391–12,419, doi:10.1002/2014JD022094, 2014.
- 862 Hervig, M. E., Siskind, D. E., Bailey, S. M., Merkel, A. W., DeLand, M. T. and Russell,
- 863 J. M.: The missing solar cycle response of the polar summer mesosphere, *Geophys. Res.*
- 864 *Lett.*, 2019GL083485, doi:10.1029/2019GL083485, 2019.
- 865 Holmen, S. E., Dyrland, M. E. and Sigernes, F.: Mesospheric temperatures derived from
- 866 three decades of hydroxyl airglow measurements from Longyearbyen, Svalbard (78°N),
- 867 *Acta Geophys.*, 62(2), 302–315, doi:10.2478/s11600-013-0159-4, 2014.
- 868 Huang, T.-Y.: Influences of CO<sub>2</sub> increase, solar cycle variation, and geomagnetic activity
- 869 on airglow from 1960 to 2015, *J. Atmos. Solar-Terrestrial Phys.*, 171, 164–175,
- 870 doi:10.1016/J.JASTP.2017.06.008, 2018.
- 871 Jacobi, C., Lilienthal, F., Geißler, C. and Krug, A.: Long-term variability of mid-latitude
- 872 mesosphere-lower thermosphere winds over Collm (51°N, 13°E), *J. Atmos. Solar-*
- 873 *Terrestrial Phys.*, 136, 174–186, doi:10.1016/j.jastp.2015.05.006, 2015.
- 874 Kalicinsky, C., Knieling, P., Koppmann, R., Offermann, D., Steinbrecht, W. and Wintel,
- 875 J.: Long-term dynamics of OH \* temperatures over central Europe: trends and solar
- 876 correlations, *Atmos. Chem. Phys.*, 16(23), 15033–15047, doi:10.5194/acp-16-15033-
- 877 2016, 2016.
- 878 Kalicinsky, C., Peters, D. H. W., Entzian, G., Knieling, P. and Matthias, V.:
- 879 Observational evidence for a quasi-bidecadal oscillation in the summer mesopause region
- 880 over Western Europe, *J. Atmos. Solar-Terrestrial Phys.*, 178, 7–16,
- 881 doi:10.1016/j.jastp.2018.05.008, 2018.



- 882 Karlsson, B. and Shepherd, T. G.: The improbable clouds at the edge of the atmosphere,  
 883 Phys. Today, 71(6), 30–36, doi:10.1063/PT.3.3946, 2018.
- 884 Kim, G., Kim, J.-H., Kim, Y. H. and Lee, Y. S.: Long-term trend of mesospheric  
 885 temperatures over Kiruna (68°N, 21°E) during 2003–2014, J. Atmos. Solar-Terrestrial  
 886 Phys., 161, 83–87, doi:10.1016/j.jastp.2017.06.018, 2017.
- 887 Kvifte, G. and G.: Temperature measurements from OH bands, Planet. Space Sci., 5(2),  
 888 153–157, doi:10.1016/0032-0633(61)90090-3, 1961.
- 889 Langhoff, S. R., Werner, H. J. and Rosmus, P.: Theoretical Transition Probabilities for  
 890 the OH Meinel System, J. Mol. Spectrosc., 118, 507–529, 1986.
- 891 Laštovička, J.: A review of recent progress in trends in the upper atmosphere, J. Atmos.  
 892 Solar-Terrestrial Phys., 163, 2–13, doi:10.1016/j.jastp.2017.03.009, 2017.
- 893 Liu, G. and Shepherd, G. G.: An empirical model for the altitude of the OH nightglow  
 894 emission, Geophys. Res. Lett., 33(9), L09805, doi:10.1029/2005GL025297, 2006.
- 895 van der Loo, M. P. J. and Groenenboom, G. C.: Theoretical transition probabilities for the  
 896 OH Meinel system, J. Chem. Phys., 126(11), 114314, doi:10.1063/1.2646859, 2007.
- 897 Livesey, N. J., Read, W. G., Wagner, P. A., Froidevaux, L., Lambert, A., Manney, G.L.,  
 898 Millán Valle, L. F., Pumphrey, H. C., Santee, M. L., Schwartz, M. J., Wang, S., Fuller, R.  
 899 A., Jarnot, R. F., Knosp, B. W., Martinez, E., Lay, R. R.: Earth Observing System (EOS)  
 900 Aura Microwave Limb Sounder (MLS) Version4.2x Level 2 data quality and description  
 901 document Version 4.2x–3.1, Jet Propulsion Laboratory, California Institute of  
 902 Technology Pasadena, California, 91109-8099, [https://mls.jpl.nasa.gov/data/v4-](https://mls.jpl.nasa.gov/data/v4-2_data_quality_document.pdf)  
 903 [2\\_data\\_quality\\_document.pdf](https://mls.jpl.nasa.gov/data/v4-2_data_quality_document.pdf), 2018.
- 904 López-Puertas, M., Funke, B., Jurado-Navarro, A., García-Comas, M., Gardini, A.,  
 905 Boone, C. D., Rezac, L. and Garcia, R. R.: Validation of the MIPAS CO<sub>2</sub> volume mixing  
 906 ratio in the mesosphere and lower thermosphere and comparison with WACCM



- 907 simulations, *J. Geophys. Res.*, 122(15), 8345–8366, doi:10.1002/2017JD026805, 2017.
- 908 Lübken, F.-J., Berger, U. and Baumgarten, G.: Temperature trends in the midlatitude
- 909 summer mesosphere, *J. Geophys. Res. Atmos.*, 118(24), 13,347–13,360,
- 910 doi:10.1002/2013JD020576, 2013.
- 911 Mertens, C. J., Mlynczak, M. G., López-Puertas, M., Wintersteiner, P. P., Picard, R. H.,
- 912 Winick, J. R., Gordley, L. L. and Russell III, J. M.: Retrieval of kinetic temperature and
- 913 carbon dioxide abundance from nonlocal thermodynamic equilibrium limb emission
- 914 measurements made by the SABER experiment on the TIMED satellite, in *Proc SPIE*
- 915 4882, *Remote Sensing of Clouds and the Atmosphere VII*, pp. 162–171., 2003.
- 916 Mies, F. H.: Calculated vibrational transition probabilities of OH(X<sup>2</sup>Π), *J. Mol.*
- 917 *Spectrosc.*, 53(2), 150–188, doi:10.1016/0022-2852(74)90125-8, 1974.
- 918 Mulligan, F. J., Dyrland, M. E., Sigernes, F. and Deehr, C. S.: Inferring hydroxyl layer
- 919 peak heights from ground-based measurements of OH(6-2) band integrated emission rate
- 920 at Longyearbyen (78°N, 16°E), *Ann. Geophys.*, 27(11), 4197–4205,
- 921 doi:10.5194/angeo-27-4197-2009, 2009.
- 922 Murphy, D. J., French, W. J. R. and Vincent, R. A.: Long-period planetary waves in the
- 923 mesosphere and lower thermosphere above Davis, Antarctica, *J. Atmos. Solar-Terrestrial*
- 924 *Phys.*, 69(17–18), 2118–2138, doi:10.1016/J.JASTP.2007.06.008, 2007.
- 925 Nath, O. and Sridharan, S.: Long-term variabilities and tendencies in zonal mean
- 926 TIMED–SABER ozone and temperature in the middle atmosphere at 10–15°N, *J. Atmos.*
- 927 *Solar-Terrestrial Phys.*, 120, 1–8, doi:10.1016/j.jastp.2014.08.010, 2014.
- 928 Offermann, D., Jarisch, M., Donner, M., Steinbrecht, W. and Semenov, A. I.: OH
- 929 temperature re-analysis forced by recent variance increases, *J. Atmos. Solar-Terrestrial*
- 930 *Phys.*, 68(17), 1924–1933, doi:10.1016/J.JASTP.2006.03.007, 2006.
- 931 Perminov, V. I., Semenov, A. I., Medvedeva, I. V. and Pertsev, N. N.: Temperature



- 932 variations in the mesopause region according to the hydroxyl-emission observations at  
 933 midlatitudes, *Geomagn. Aeron.*, 54(2), 230–239, doi:10.1134/S0016793214020157,  
 934 2014.
- 935 Perminov, V. I., Semenov, A. I., Pertsev, N. N., Medvedeva, I. V., Dalin, P. A. and  
 936 Sukhodoev, V. A.: Multi-year behaviour of the midnight OH\* temperature according to  
 937 observations at Zvenigorod over 2000–2016, *Adv. Sp. Res.*, 61(7), 1901–1908,  
 938 doi:10.1016/J.ASR.2017.07.020, 2018.
- 939 Pertsev, N. and Perminov, V.: Response of the mesopause airglow to solar activity  
 940 inferred from measurements at Zvenigorod, Russia, *Ann. Geophys.*, 26(5), 1049–1056,  
 941 doi:10.5194/angeo-26-1049-2008, 2008.
- 942 Qian, L., Jacobi, C. and McInerney, J.: Trends and Solar Irradiance Effects in the  
 943 Mesosphere, *J. Geophys. Res. Sp. Phys.*, 124(2), 1343–1360,  
 944 doi:10.1029/2018JA026367, 2019.
- 945 Randall, C. E., Harvey, V. L., Siskind, D. E., France, J., Bernath, P. F., Boone, C. D. and  
 946 Walker, K. A.: NO<sub>x</sub> descent in the arctic middle atmosphere in early 2009,  
 947 *Geophys. Res. Lett.*, 36(18), doi:10.1029/2009GL039706, 2009.
- 948 Reid, I. M., Spargo, A. J., Woithe, J. M., Klekociuk, A. R., Younger, J. P. and Sivjee, G.  
 949 G.: Seasonal MLT-region nightglow intensities, temperatures, and emission heights at a  
 950 Southern Hemisphere midlatitude site, *Ann. Geophys.*, 35(3), 567–582,  
 951 doi:10.5194/angeo-35-567-2017, 2017.
- 952 Reisin, E. R., Scheer, J., Dyrland, M. E., Sigernes, F., Deehr, C. S., Schmidt, C.,  
 953 Höppner, K., Bittner, M., Ammosov, P. P., Gavriljeva, G. A., Stegman, J., Perminov, V.  
 954 I., Semenov, A. I., Knieling, P., Koppmann, R., Shiokawa, K., Lowe, R. P., López-  
 955 González, M. J., Rodríguez, E., Zhao, Y., Taylor, M. J., Buriti, R. A., Espy, P. J., French,  
 956 W. J. R., Eichmann, K.-U., Burrows, J. P. and von Savigny, C.: Traveling planetary wave



957 activity from mesopause region airglow temperatures determined by the Network for the  
 958 Detection of Mesospheric Change (NDMC), *J. Atmos. Solar-Terrestrial Phys.*, 119, 71–  
 959 82, doi:10.1016/J.JASTP.2014.07.002, 2014.

960 Rezac, L., Jian, Y., Yue, J., Russell, J. M., Kutepov, A., Garcia, R., Walker, K. and  
 961 Bernath, P.: Validation of the global distribution of CO<sub>2</sub> volume mixing ratio in the  
 962 mesosphere and lower thermosphere from SABER, *J. Geophys. Res.*, 120(23), 12,067–  
 963 12,081, doi:10.1002/2015JD023955, 2015.

964 Rezac, L., Yue, J., Yongxiao, J., Russell, J. M., Garcia, R., López-Puertas, M. and  
 965 Mlynarczyk, M. G.: On Long-Term SABER CO<sub>2</sub> Trends and Effects Due to Nonuniform  
 966 Space and Time Sampling, *J. Geophys. Res. Sp. Phys.*, 123(9), 7958–7967,  
 967 doi:10.1029/2018JA025892, 2018.

968 Roble, R. G.: On the feasibility of developing a global atmospheric model extending from  
 969 the ground to the exosphere, pp. 53–67., 2000.

970 Roble, R. G. and Dickinson, R. E.: How will changes in carbon dioxide and methane  
 971 modify the mean structure of the mesosphere and thermosphere?, *Geophys. Res. Lett.*,  
 972 16(12), 1441–1444, doi:10.1029/GL016i012p01441, 1989.

973 von Savigny, C.: Variability of OH(3–1) emission altitude from 2003 to 2011: Long-term  
 974 stability and universality of the emission rate–altitude relationship, *J. Atmos. Solar-*  
 975 *Terrestrial Phys.*, 127, 120–128, doi:10.1016/J.JASTP.2015.02.001, 2015.

976 von Savigny, C., McDade, I. C., Eichmann, K. U. and Burrows, J. P.: On the dependence  
 977 of the OH\* Meinel emission altitude on vibrational level: SCIAMACHY observations  
 978 and model simulations, *Atmospheric Chem. Phys.*, 12, 8813–8828, doi:10.5194/acp-12-  
 979 8813-2012, 2012.

980 Scheer, J., Reisin, E. R. and Mandrini, C. H.: Solar activity signatures in mesopause  
 981 region temperatures and atomic oxygen related airglow brightness at El Leoncito,



- 982 Argentina, J. Atmos. Solar-Terrestrial Phys., 67(1–2), 145–154,
- 983 doi:10.1016/j.jastp.2004.07.023, 2005.
- 984 Schmidt, H., Brasseur, G. P., Charron, M., Manzini, E., Giorgetta, M. A., Diehl, T.,
- 985 Fomichev, V. I., Kinnison, D., Marsh, D. and Walters, S.: The HAMMONIA chemistry
- 986 climate model: Sensitivity of the mesopause region to the 11-year solar cycle and CO<sub>2</sub>
- 987 doubling, J. Clim., 19(16), 3903–3931, doi:10.1175/JCLI3829.1, 2006.
- 988 Schwartz, M. J., Lambert, A., Manney, G. L., Read, W. G., Livesey, N. J., Froidevaux,
- 989 L., Ao, C. O., Bernath, P. F., Boone, C. D., Cofield, R. E., Daffer, W. H., Drouin, B. J.,
- 990 Fetzer, E. J., Fuller, R. A., Jarnot, R. F., Jiang, J. H., Jiang, Y. B., Knosp, B. W., Krüger,
- 991 K., Li, J.-L. F., Mlynczak, M. G., Pawson, S., Russell, J. M., Santee, M. L., Snyder, W.
- 992 V., Stek, P. C., Thurstans, R. P., Tompkins, A. M., Wagner, P. A., Walker, K. A., Waters,
- 993 J. W. and Wu, D. L.: Validation of the Aura Microwave Limb Sounder temperature and
- 994 geopotential height measurements, J. Geophys. Res., 113(D15),
- 995 doi:10.1029/2007jd008783, 2008.
- 996 Sivakandan, M., Ramkumar, T. K., Taori, A., Rao, V. and Niranjana, K.: Long-term
- 997 variation of OH peak emission altitude and volume emission rate over Indian low
- 998 latitudes, J. Atmos. Solar-Terrestrial Phys., 138–139, 161–168,
- 999 doi:10.1016/j.jastp.2016.01.012, 2016.
- 1000 Sivjee, G. G.: Airglow hydroxyl emissions, Planet. Space Sci., 40(2–3), 235–242,
- 1001 doi:10.1016/0032-0633(92)90061-R, 1992.
- 1002 Solomon, S. C., Liu, H., Marsh, D. R., McInerney, J. M., Qian, L. and Vitt, F. M.: Whole
- 1003 Atmosphere Simulation of Anthropogenic Climate Change, Geophys. Res. Lett., 45(3),
- 1004 1567–1576, doi:10.1002/2017GL076950, 2018.
- 1005 Sonnemann, G. R., Hartogh, P., Berger, U. and Grygalashvily, M.: Hydroxyl layer: trend
- 1006 of number density and intra-annual variability, Ann. Geophys., 33(6), 749–767,



- 1007 doi:10.5194/angeo-33-749-2015, 2015.
- 1008 Tang, C., Liu, D., Wei, H., Wang, Y., Dai, C., Wu, P., Zhu, W. and Rao, R.: The
- 1009 response of the temperature of cold-point mesopause to solar activity based on SABER
- 1010 data set, *J. Geophys. Res. Sp. Phys.*, 121(7), 7245–7255, doi:10.1002/2016JA022538,
- 1011 2016.
- 1012 Teiser, G. and von Savigny, C.: Variability of OH(3-1) and OH(6-2) emission altitude
- 1013 and volume emission rate from 2003 to 2011, *J. Atmos. Solar-Terrestrial Phys.*, 161, 28–
- 1014 42, doi:10.1016/J.JASTP.2017.04.010, 2017.
- 1015 Thulasiraman, S. and Nee, J. B.: Further evidence of a two-level mesopause and its
- 1016 variations from UARS high-resolution Doppler imager temperature data, *J. Geophys.*
- 1017 *Res.*, 107(D18), 4355, doi:10.1029/2000JD000118, 2002.
- 1018 Turnbull, D. N. and Lowe, R. P.: New hydroxyl transition probabilities and their
- 1019 importance in airglow studies, *Planet. Space Sci.*, 37(6), 723–738, doi:10.1016/0032-
- 1020 0633(89)90042-1, 1989.
- 1021 Venturini, M. S., Bageston, J. V., Caetano, N. R., Peres, L. V., Bencherif, H. and Schuch,
- 1022 N. J.: Mesopause region temperature variability and its trend in southern Brazil, *Ann.*
- 1023 *Geophys.*, 36(2), 301–310, doi:10.5194/angeo-36-301-2018, 2018.
- 1024 Wüst, S., Bittner, M., Yee, J.-H., Mlynczak, M. G. and Russell III, J. M.: Variability of
- 1025 the Brunt–Väisälä frequency at the OH\* layer height, *Atmos. Meas. Tech.*, 10(12), 4895–
- 1026 4903, doi:10.5194/amt-10-4895-2017, 2017.
- 1027 Xu, J., Liu, H.-L., Yuan, W., Smith, A. K., Roble, R. G., Mertens, C. J., Russell, J. M.
- 1028 and Mlynczak, M. G.: Mesopause structure from Thermosphere, Ionosphere,
- 1029 Mesosphere, Energetics, and Dynamics (TIMED)/Sounding of the Atmosphere Using
- 1030 Broadband Emission Radiometry (SABER) observations, *J. Geophys. Res.*, 112(D9),
- 1031 D09102, doi:10.1029/2006JD007711, 2007.



- 1032 Yuan, T., Solomon, S. C., She, C. -Y., Krueger, D. A. and Liu, H. -L.: The long-term  
1033 trends of nocturnal mesopause temperature and altitude revealed by Na lidar observations  
1034 between 1990 and 2018 at mid-latitude, *J. Geophys. Res. Atmos.*, 2018JD029828,  
1035 doi:10.1029/2018JD029828, 2019.
- 1036 Yue, J., Russell, J., Jian, Y., Rezac, L., Garcia, R., López-Puertas, M. and Mlynczak, M.  
1037 G.: Increasing carbon dioxide concentration in the upper atmosphere observed by  
1038 SABER, *Geophys. Res. Lett.*, 42(17), 7194–7199, doi:10.1002/2015GL064696, 2015.
- 1039 von Zahn, U., Höffner, J., Eska, V. and Alpers, M.: The mesopause altitude: Only two  
1040 distinctive levels worldwide?, *Geophys. Res. Lett.*, 23(22), 3231–3234,  
1041 doi:10.1029/96GL03041, 1996.
- 1042